Matter and Radiation at Extremes | RESEARCH ARTICLE | scitation.org/journal/mre

Stark–Zeeman line-shape model for multi-electron radiators in hot dense plasmas subjected to large magnetic fields

Cite as: Matter Radiat. Extremes 7, 015901 (2022); doi: 10.1063/5.0058552
Submitted: 31 May 2021 • Accepted: 3 November 2021 •
Published Online: 2 December 2021

Sandrine Ferri,[a] Olivier Peyrusse, and Annette Calisti

AFFILIATIONS

Aix-Marseille Université, CNRS, PIIM, UMR7345, Marseille, France

Note: This paper is part of the Special Issue on Magnetized Plasmas in HED.
[a]**Author to whom correspondence should be addressed:** sandrine.ferri@univ-amu.fr

ABSTRACT

We present a Stark–Zeeman spectral line-shape model and the associated numerical code, PPPB, designed to provide fast and accurate line shapes for arbitrary atomic systems for a large range of plasma conditions. PPPB is based on the coupling of the PPP code—a Stark-broadened spectral line-shape code developed for multi-electron ion spectroscopy in hot dense plasmas—and the MASCB code developed recently to generate B-field-dependent atomic physics. The latter provides energy levels, statistical weights, and reduced matrix elements of multi-electron radiators by diagonalizing the atomic Hamiltonian that includes the well know B-dependent term. These are then used as inputs to PPP working in the standard line-broadening approach, i.e., using the quasi-static ion and impact electron approximations. The effects of ion dynamics are introduced by means of the frequency fluctuation model, and the physical model of electron broadening is based on the semi-classical impact approximation including the effects of a strong collision term, interference, and cyclotron motion. Finally, to account for polarization effects, the output profiles are calculated for a given angle of observation with respect to the direction of the magnetic field. The potential of this model is presented through Stark–Zeeman spectral line-shape calculations performed for various experimental conditions.

I. INTRODUCTION

Measurements of magnetic fields are important in many studies of laboratory or space plasmas. Among other methods, spectroscopic measurements are often used in plasmas to infer (i) temperatures from line intensity ratios and Doppler broadening, (ii) electron densities from Stark broadening, and (iii) magnetic field strengths from distinct line-shape features. Spectroscopic diagnostic techniques are based on comparing observed and modeled spectra, so implementing them reliably requires accurate calculations of emission or absorption spectra, implying the use of analytic methods and computer codes of differing complexity and applicability limits. Line-shape modeling in plasmas has a long history,[1] but the existence of intense magnetic fields in astrophysical objects (e.g., white dwarfs) and various types of plasmas created in the laboratory (e.g., magnetic- and inertial-confinement fusion devices) has revived interest in atomic-physics developments for such extreme conditions.

The presence of magnetic fields increases the complexity of line-shape calculations in plasmas. A magnetic field has three essential effects on Stark-broadened spectral lines: (i) partial polarization of the emitted light, (ii) additional splitting according to the value of the magnetic quantum number m, and (iii) bending the colliding charged-particle trajectories into a helical path around the magnetic lines of force. These effects have been studied both theoretically and experimentally for several decades since the initial work of Nguyen-Hoe *et al.*[2] Different methods have been either developed for or extended to magnetized plasmas, such as numerical simulations[3–6] and various theoretical models.[7–16] Most of these are based on simplifying assumptions depending on the relative importance of the Stark and Zeeman effects, a measure of which is given by the ratio τ between their respective average energy shifts.[2] For example, for hydrogen and with the normal electric field strength $F_0 = e/r_e^2$ and $r_e = \left(\frac{3}{4\pi N_e}\right)^{1/3}$, where e is the elementary charge and N_e (cm^{-3}) is the electron density, τ is given by

$$\tau = 5.15 \times 10^{-11} n N_e^{2/3} / B, \quad (1)$$

where n is the principal quantum number (PQN) and B (T) is the magnetic field strength. The line profile coincides with the pure Stark

profile if $\tau \gg 1$ and deviates progressively as τ decreases. When $\tau \sim 1$, a profile broadened by the combined Stark–Zeeman (SZ) effect is an intricate function of N_e and B. Such cases are found in (i) low-n hydrogen line series emitted in tokamak edge regions where $N_e \sim 10^{14}$ cm^{-3}, $T_e \sim 1$ eV, and B is a few teslas or (ii) white dwarfs, where the signature of intense magnetic fields (over a few hundred teslas) is observed at higher densities ($N_e \sim 10^{17}$ cm^{-3}). In laser-produced plasmas (T_e between 100 eV and 1 keV and N_e between 10^{21} cm^{-3} and 10^{24} cm^{-3}), high magnetic fields of over a few hundred teslas are generated and can have a strong effect on the emission of highly ionized atoms.[17,18] These conditions require the Stark and Zeeman effects on line broadening to be treated simultaneously.

The goal of the present work is to present the main features of the SZ line-shape code PPPB through various applications related to strongly magnetized plasmas.

II. ATOMIC PHYSICS IN PRESENCE OF MAGNETIC FIELDS

The atomic data necessary for an SZ calculation are usually generated by atomic-physics codes free of any external field. In practice, we use the Cowan–Hartree–Fock atomic-structure code,[19] the multiconfiguration Dirac–Fock code (MCDF),[20] the Flexible Atomic Code (cFAC),[21,22] or homemade codes for neutrals. In its original form, PPPB was designed to solve the problem within the approximation of a strong or weak magnetic field. The energy levels, statistical weights, and reduced dipole matrix elements were generated externally, and the Zeeman contribution to the Hamiltonian was introduced in PPPB neglecting the quadratic contribution.

The Zeeman Hamiltonian reads as

$$H_Z = \mu_B B(L_z + g_s S_z), \tag{2}$$

where B is the magnitude of the magnetic field in the z direction, μ_B is the Bohr magneton, $g_s = 2.002\,319\,2$ is the anomalous gyromagnetic ratio for the electron spin, and L_z and S_z are the projections of the total orbital and spin angular momenta of the atom, respectively. For sufficiently weak B-field values, the off-diagonal matrix elements of H_Z that connect states of different values of the modulus J of the total angular momentum of the system, $\vec{J} \to \vec{L} + \vec{S}$, are negligible compared to the contributions of the Coulomb and spin–orbit interactions. The contribution of the magnetic field to the energy can be calculated as a perturbation. The following expression of the diagonal matrix element of H_Z for the state $|\gamma\ J\ M\rangle$ was retained in PPPB:

$$\langle \gamma\ J\ M|(L_z + g_s S_z)|\gamma\ J\ M\rangle = g_{\gamma J} M, \tag{3}$$

where $g_{\gamma J}$ is the Landé factor of the level $\gamma\ J$.[19] For magnetic fields sufficiently strong to disrupt the coupling between the orbital $\vec{L}$ and spin $\vec{S}$ momenta, L_z and S_z are easily evaluated for a state $|\gamma\ L\ S\ m_l\ m_s\rangle$. The strong-field approximation through the following expression was then retained:

$$\langle \gamma\ L\ S\ m_l\ m_s|(L_z + g_s S_z)|\gamma\ L\ S\ m_l\ m_s\rangle = m_l + g_s m_s. \tag{4}$$

One can consider the weak- and strong-field approaches to be no longer valid when the magnetic field and the spin–orbit contributions are of the same order of magnitude. In this intermediate case, the whole Hamiltonian $\xi \vec{L} \cdot \vec{S} + \mu_B \vec{B}(\vec{L} + g_s \vec{S})$ must be diagonalized.

For the one-electron configuration, the critical B-field value B_c (T) at which both contributions must be considered at the same level in the Hamiltonian is estimated as[23]

$$B_c \sim \left(\frac{Z^*}{n}\right)^4 \left(\frac{e^2}{\hbar c}\right)^2 \frac{m_e e^4}{\mu_B \hbar^2}, \tag{5}$$

where Z^* is the effective charge given by Slater's rule, i.e., $Z^* = Z - \sigma$, where σ is the screening constant.[24] Table I gives the values of B_c for some H-like ($Z^* = Z$) and Li-like ($Z^* = Z - 2\sigma_{1s}$, with $\sigma_{1s} = 0.85$) ions of interest, with radiative transitions from $n = 2$ assumed.

To go beyond the aforementioned weak- and strong-field approximations, the atomic-physics code MASCB has been developed to generate B-field-dependent atomic-physics quantities. MASCB follows the usual approach in which the N-electron atomic Hamiltonian H is divided into two parts: a separable part in which electrons are supposed to be independent in a central potential, and a corrective part that is treated using perturbation theory. In this framework, multi-electron atomic states appear formally as a combination of Slater determinants. This means that the matrix elements of H, J^2, and J_z must be calculated, and the eigenvectors of these operators obtained after diagonalization are the eigenstates of the atomic system. After identifying the useful (i.e., restricted; see Refs. 25 and 26, for instance) Slater determinant belonging to a set of configurations, matrix elements are calculated using the Condon rules summarized in classical textbooks.[24,27] The restriction of the Slater determinant set involves considering just one possible value of M (eigenvalue of J_z) that is common to all states of a set of configurations. The subsequent calculations of transition matrix elements coupling states of different M make use of the Wigner–Eckart theorem and of operator J_+ or J_- when needed. After treating a list of configurations sequentially, it is still possible to diagonalize the atomic Hamiltonian on the basis of the states belonging to all of the considered configurations, which is just the method known as superposition of configurations.

The description is non-relativistic, i.e., based on the Schrödinger equation, but it incorporates the main relativistic corrections to the central-field potential.[19] This central potential—from which mono-electronic energies and orbitals are obtained self-consistently—is built in the framework of the optimized effective potential.[28,29]

After the primary treatment of an *isolated* atom, one diagonalizes the part of the Hamiltonian describing the interaction with the magnetic field. This part reads (in SI units)

$$H_B = H_Z + \frac{e^2 B^2}{8 m_e} \sum_i^N r_i^2 \sin^2\theta_i, \tag{6}$$

TABLE I. Critical values of magnetic field at which spin–orbit interaction is of same order of magnitude as magnetic interaction. Estimations are for hydrogen-like and lithium-like ionization stages of elements of interest in this work.

Element	B_c (T)	
	H-like	Li-like
H ($Z = 1$)	0.78	⋯
C ($Z = 6$)	10^3	270
Si ($Z = 14$)	30×10^3	18×10^3
Ar ($Z = 18$)	80×10^3	55×10^3

where H_Z is the linear Zeeman term [Eq. (2)] and the second term is the quadratic term. Here, r_i and θ_i are the usual polar coordinates of electron i in a system in which the polar axis is along the B axis, i.e., the z axis.[30]

Note that the quadratic term of H_B introduces mixing among states of different n, making the matrix of infinite order. Therefore, the eigenvalues are necessarily approximated by those of a truncated Hamiltonian matrix for H_B, truncated because this matrix is limited to a preselected set of configurations. For a given value of the magnetic field, it is then necessary to check whether adding more configurations changes the eigenvalues of interest significantly. For hydrogen or helium atoms, this method has been shown to yield sufficiently accurate results.[30] Figure 1 shows how the quadratic terms affect the Balmer-series lines of hydrogen (up to $H-\varepsilon$ corresponding to the radiative transition from $n = 7$ to $n = 2$)[31,32] for plasma conditions relevant to white-dwarf atmospheres.[33] We compare the SZ profiles obtained with and without the quadratic B-field effects for three magnetic-field values: B = (a) 100 T, (b) 500 T, and (c) 1 kT. The calculations were performed over the entire Balmer series at once, accounting for Stark coupling between upper levels with different PQNs. Note that our atomic-structure calculation is performed in a configuration interaction mode in which the mixing is introduced by the quadratic term; this point is crucial for proper consideration of this term.

The quadratic terms give rise to additional structures in the line shapes and to a global shift that increases with the PQN. For higher magnetic fields, the Zeeman components from different PQNs merge so that the line series resembles a complex set of indiscernible lines. Inferring the B-field from those lines is no longer possible.

Also, using the Inglis–Teller limit[34] to measure the electron density can overestimate the latter if Zeeman effects are not considered in the calculation. For example, the largest PQN given by the Inglis–Teller limit is nearly 7 for an electron density of 10^{17} cm^{-3}. The SZ Balmer series verifies this limit for a magnetic field of the order of 100 T, but the lines emitted for large quantum numbers start to merge as the B-field increases. For B = 500 T, the lines resolved last correspond to the H_δ transitions, i.e., from the upper level of $n = 6$; using this level as the largest PQN to infer the electron density would give $N_e \sim 2.7 \times 10^{17}$ cm^{-3} instead of $N_e = 10^{17}$ cm^{-3} as calculated. For B = 1 kT, the lines resolved last correspond to the H_γ transitions, i.e., from the upper level of $n = 5$; therefore, the corresponding inferred electron density would be $N_e = 10^{18}$ cm^{-3}, an order of magnitude higher than the correct value.

III. HELICAL TRAJECTORIES

Another difficulty to overcome in magnetized plasmas is that charged particles follow helical trajectories, and this gyromotion of electrons and ions around the magnetic lines of force may alter the dynamics of the plasma particles. Recent studies in strongly coupled magnetized plasmas—i.e., when the Coulomb interaction exceeds the kinetic energy of the particles—have reported a strong influence of the helical trajectories on the transport properties.[35–37] A significantly curved trajectory will also change the emitter–perturber interaction dynamics. Of particular current interest are the electric microfield statistical properties in the case of strongly magnetized plasmas, whereby the SZ broadening mechanisms of spectral line shape could be affected.

The effect of helical trajectories on the emitter–perturber interaction can be estimated from the ratio of the Debye length

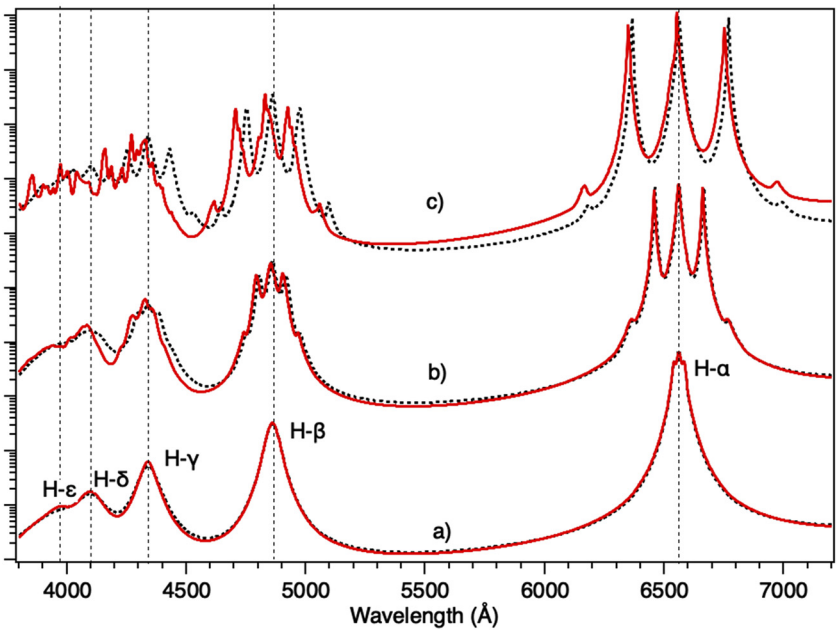

FIG. 1. Stark–Zeeman (SZ)-broadened Balmer-series lines for $N_e = 10^{17}$ cm^{-3}, $T_e = 5$ eV, and B = (a) 100 T, (b) 500 T, and (c) 1 kT with (solid) and without (dashed) quadratic terms. The direction of observation is transverse to the B-field direction.

TABLE II. Electron density N_e and critical B-field B_h for electrons in plasmas of interest (with values of magnetic field commonly measured in these plasmas).

Magnetized plasmas	N_e (cm^{-3})	B_h (T)
Tokamak edge plasmas ($B \sim$ a few teslas)	10^{13}	1
White dwarf ($B \sim$ 100 T to 1 kT)	10^{17}	100
Laser plasmas ($B <$ 500 T)	10^{20}	3.2×10^3
Imploded targets ($B \sim$ a few kiloteslas)	10^{23}	100×10^3

$\lambda_D = \sqrt{\frac{k_B T}{4\pi N_e e}}$ to the Larmor radius $r_L = \sqrt{k_B T mc^2}/ZeB$, where m, T, and Z are the particle mass, temperature, and charge, respectively. When the Larmor radius is of the same order as the Debye length, the perturber gyration occurs on the same time and length scales as those of the Coulomb interaction. Above a critical B-field B_h, which corresponds to $\lambda_D/r_L = 1$, the helical trajectories must then be accounted for. By way of illustration, values of the critical B-field for electrons in magnetized plasmas of interest are summarized in Table II.

Recent studies of how B-fields influence electron trajectories in hydrogen plasmas have been performed in the context of magnetic fusion and white dwarfs.[38–41] It has been shown that introducing helical trajectories reduces the characteristic duration of the perturbation to the order of the inverse of the Larmor frequency, i.e., $\tau_L = 2\pi/\omega_L = 2\pi m_e c/eB$, which results in line-shape narrowing. Such results suggest a modification of the electron collision operator generally used to describe the electronic Stark effect in line-shape modeling, as will be seen in Sec. IV C.

Regarding how helical trajectories affect the interaction between the radiator and ionic perturbers, investigations of the statistical properties of ionic microfields using classical molecular dynamics (MD) simulations have been performed for short-pulse laser experimental conditions in which magnetic fields of a few thousand teslas have been measured.[3] It has been shown that the modification of the ionic field distribution function $W(F)$ by the magnetic field is negligible, and Deutsch[42] drew the same conclusion: "The low-frequency component of the electric microfields is seen to be rigorously unaffected by magnetic field in a thermal plasma," but to conclude: "in presence of a very strong magnetic field $(\cdots)$ the slow electrons are to be added to the ionic part of the low-frequency component." Very recent MD simulations[43] in the context of high-B-field generation using laser–plasma interactions[17] have shown that the helical trajectories of the electrons along the B-lines of force may affect the distribution of the electrons around the ions and thus may indirectly affect the ionic microfield distribution functions; however, such results are preliminary and more investigations are required.

IV. PPPB: A STARK–ZEEMAN LINE-SHAPE CODE

The spectral line-shape code PPPB has been designed to provide SZ-broadened line shapes for wide ranges of density, temperature, and magnetic field.[14] It is based on the PPP code, a Stark-broadened spectral line-shape code[44,45] developed some years ago for multi-electron ion spectroscopy in inertial-confinement-fusion plasmas.[46,47]

Line shapes are usually modeled by working in the "standard" quasi-static ion/impact electron limit. The line-shape function is given by

$$I_s(\omega) = \int_0^\infty W(F_i) I(\omega, F_i)\, \mathrm{d}F_i, \tag{7}$$

where ω is the photon frequency and $I(\omega, F_i)$ is the electron-broadened line profile for a given value of the microfield F_i following the static ion microfield distribution function $W(F_i)$. The field-dependent profile reads as

$$I(\omega, F_i) = \frac{1}{\pi} \mathrm{ReTr}\{d^\dagger [i\omega - iL(F_i) + \phi(\omega)]^{-1} \rho d\}, \tag{8}$$

where $L(F_i) = [H_Z(F_i), I]$ is the Liouville operator associated with the B-field-dependent Hamiltonian of the emitter H_Z, ρ is the emitter density operator, d is the emitter dipole operator, and $\phi(\omega)$ is the electron-broadening operator (see Sec. IV C).

A peculiarity of the Zeeman effect is a quantization axis imposed by the magnetic field. This implies that the emission is polarized, following the selection rules for the dipole radiation—$\Delta J = J' - J = 0, \pm 1$ ($J' = J = 0$ not allowed), $q = \Delta M = M' - M = \pm 1$ ($\sigma_\pm$ polarizations), and $q = \Delta M = 0$ (π polarizations)—assuming that the magnetic field is in the z direction. Because the symmetry is broken, integrating over the ionic microfield implies considering the three spatial directions separately. One defines $\vec{F}_\parallel$ and $\vec{F}_\perp$ as the ionic microfields parallel and perpendicular to the direction of the magnetic field, respectively. If θ is the angle between the magnetic and electric fields, then we have $F_\parallel = F_i \mu$ and $F_\perp = F_i \sqrt{1-\mu^2}$, with $\mu = \cos\theta$. Therefore, the line profile given by Eq. (7) is written as

$$I_{s,q}(\omega) = \frac{1}{2} \int_0^\infty W(F_i) \int_{-1}^{+1} I_q(\omega, F_i, \mu)\, \mathrm{d}\mu \mathrm{d}F_i, \tag{9}$$

where $I_q(\omega, F_i, \mu)$ represents the q-polarized line profile emitted by an ion in an external magnetic field and in a static ion field F_i.

The emission profile observed in the line of sight of the observer is given by

$$I(\omega, \alpha) = I_\parallel(\omega) \cos^2(\alpha) + I_\perp(\omega) \sin^2(\alpha), \tag{10}$$

where α is the angle between the line of sight of the observer and the direction of $\vec{B}$, and

$$I_\parallel(\omega) = I_{+1}(\omega) + I_{-1}(\omega), \tag{11}$$

$$I_\perp(\omega) = I_0(\omega) + \frac{1}{2}(I_{+1}(\omega) + I_{-1}(\omega)), \tag{12}$$

where $I_{-1}(\omega)$, $I_0(\omega)$, and $I_{+1}(\omega)$ are the q-polarized components given in Eq. (9) with $q = -1, 0, +1$, respectively.

Calculating the integrand in Eq. (9) involves inverting and multiplying matrices in the complex domain. In principle, this calculation must be done for every static ion microfield point and for every frequency point in the line shape $I_s(\omega)$. This is the most time-consuming task in a line-shape code, therefore computer power and

efficient algorithms are essential to make complex emitter line-shape calculations practical.

A. Static profile and Stark-dressed transitions

The PPPB code performs block diagonalization of the resolvent in Eq. (8), afforded by the selection rules of the atomic matrix elements. It performs an eigendecomposition of the resolvent in the $\{f,\mu\}$-dependent bases (see Refs. 14, 44, and 48 for more details):

$$I_{s,q}(\omega) = \sum_f W_f^{(2)} \sum_\mu W_\mu^{(G)}\ \mathrm{Im} \times \langle\langle d_q^\dagger | M_{f,\mu} \left[\omega 1 - L^d(f,\mu)\right]^{-1} M_{f,\mu}^{-1} | d_q \rho_0 \rangle\rangle, \quad (13)$$

where $M_{f,\mu}$ is the matrix that diagonalizes the Liouville operator L: $M_{f,\mu}^{-1} L(f,\mu) M_{f,\mu} = L^d(f,\mu)$. The integrations over F_i and μ are replaced by (i) a two-point integration weight, used for the summation over the discrete ionic field intensities f, and (ii) a Gauss–Legendre quadrature weight, used for the angle summation.[49] The number of microfields necessary to describe the static distribution function well is $n_f \sim 50$, and a value of $n_\mu \sim 30$ is enough for good convergence in the angle summation.

In the PPPB code, the static microfield distribution functions are either estimated from classical MD simulations[50] or by the Adjustable Parameter EXponential (APEX) model.[51,52] The latter is computationally fast and suited for both weakly and strongly coupled plasmas. Note that the Hooper static-field distribution function is used for the calculations involving neutral emitters.[53] Accordingly, those models do not depend on B and consider the plasma that surrounds the emitter, isotrope.

This procedure leads to the concept of the Stark spectral components emitted by a set of dressed two-level radiators, i.e., the Stark-dressed transitions (SDTs). These are characterized by two complex numbers, i.e., the generalized intensity $a_{q,k} + ic_{q,k}$ and the generalized frequency $f_{q,k} + i\gamma_{q,k}$.

The static q-polarized profile is then described by a sum of rational fractions that are generalized Lorentzian spectral components of the line:

$$I_{s,q}(\omega) = \sum_{k=1}^{n_{q,k}} \frac{c_k(\omega - f_{q,k}) + a_{q,k}\gamma_{q,k}}{(\omega - f_{q,k})^2 + \gamma_{q,k}^2}, \quad (14)$$

where $n_{q,k} = n_f \times n_\mu \times n_e \times n_g$ is the number of SDTs, which is also proportional to n_g and n_e, the numbers of ground and upper selected energy levels, respectively, that define the studied atomic system.

B. Frequency fluctuation model: stochastic mixing of SDTs

The quasi-static approximation is useful, but it is well known that a quasistatic treatment of the ion perturbation can lead to large errors for plasma conditions that yield substantial microfield fluctuations.[54] Depending on the time scale of the line emission, the fluctuations of the microfields produced by the moving ions have to be accounted for. This is the most difficult part of the line-broadening problem due to the stochastic behavior of the microfields.[55]

In PPPB, the ion dynamics that produce microfield fluctuations are modeled using the frequency fluctuation model (FFM).[14,56]

This is based on the assumption that an atomic system perturbed by a fluctuating microfield behaves like a set of SDTs that are subject to a stationary Markov mixing process induced by the field fluctuation. This results in an effective exchange between two-level transitions following a Poisson process with the fluctuation rate of $\nu_i = v_{th}/r_i$, where v_{th} is the ion thermal velocity and $r_i = (\frac{4}{3}\pi N_i)^{-1/3}$ is the mean distance between the ions, assuming an ionic density N_i.

Working in the Liouville space of the SDTs, the SZ line shape accounting for the ion dynamics and polarization is written as

$$I_{d,q}(\omega) = \mathrm{Re}\frac{1}{\pi}\sum_{kj} i\langle D_{d,k} | \left(\omega 1 - L^d - i\Gamma + iW\right)^{-1} | D_{q,j}\rangle p_{q,j}, \quad (15)$$

where L^d is the Liouville operator involving the transition frequencies of the SDTs, $D_{q,j} = r_q\sqrt{1 + ic_j/a_j}$ are the matrix elements of the dipole moment for the SDTs in the q polarization state $\left(r_q^2 = \sum_k a_{q,k}\right)$, and $p_{q,j} = a_{q,j}/r_q^2$ is the instantaneous probability of state j in the q polarization state. Γ is defined as the diagonal matrix of inverse lifetimes with $\Gamma_{kj} = \nu_i\delta_{kj}$, and W is the matrix of transitions rates between different states, such as $W = \nu_i p_{q,k}$.

The particular form of W avoids matrix inversion. According to Ref. 56, defining the quasistatic propagator

$$G^s(z) = \left(z - iL^d - i\Gamma\right)^{-1} \quad (16)$$

that has only diagonal matrix elements, the total propagator can be written as

$$G^d(z) = G^s(z) - iG^s(z)\cdot W \cdot G^d(z), \quad (17)$$

and introducing the previous expression in Eq. (15), we obtain

$$I_{d,q}(\omega) = \frac{r_q^2}{\pi}\mathrm{Re}\frac{\sum_k \frac{(a_{q,k}+ic_{q,k})/r_q^2}{\nu_i+\gamma_{q,k}+i(\omega-\omega_{q,k})}}{1-\nu_i\sum_k \frac{a_{q,k}/r_q^2}{\nu_i+\gamma_{q,k}+i(\omega-\omega_{q,k})}}. \quad (18)$$

This expression is used to calculate the SZ line shape along the line of sight given by Eqs. (10)–(12).

C. Electron broadening operator

The physical model of electron broadening used in PPPB is based on a semi-classical impact approximation including the effects of a strong collision term[57] and interference.[58] It is supposed that the emitter interacts with the plasma by binary collisions considering independent pseudo-electrons. The Debye length represents an upper cutoff beyond which the electrons do not collide. Moreover, the pseudo-electrons move at constant velocities along straight trajectories. A lower cutoff is introduced to avoid the Coulomb divergence at short distances. Using perturbation theory up to second order in the emitter–electron interaction, the Maxwell-average operator is given by

$$\Phi(\Delta\omega) = -\frac{4\pi}{3}N_e\sqrt{\frac{2m_e}{\pi k_B T_e}}\left(\frac{\hbar}{m_e}\right)^2 \vec{R}\cdot\vec{R}\,(C_n + G(\Delta\omega)), \quad (19)$$

where $\Delta\omega$ is the frequency detuning from the line center, $\vec{R}$ is the (emitter) electron position operator operating in the subspace of PQN n, and C_n is the n-dependent strong collision term, with $C_2 = 1.5$, $C_3 = 1.0$, $C_4 = 0.75$, $C_5 = 0.5$, and $C_n = 0.4$ for $n > 5$.

There are many ways to estimate $G(\Delta\omega)$ (see Ref. 16 and the references therein). We use the semi-classical GBK model[57]

$$G(\Delta\omega) = \frac{1}{2}\int_y^\infty \frac{e^{-x}}{x}\,dx \text{ with } y \approx \left(\frac{\hbar n^2}{2Z}\right)^2\left(\frac{\Delta\omega^2+\omega_c^2}{E_H k_B T_e}\right), \quad (20)$$

where the cutoff frequency ω_c is linked to the upper cutoff $\rho_{\max} = v_{th}/\omega_c$ given in Eq. (15) in Ref. 57, and $v_{th} = (kT/m_e)^{1/2}$ is the average thermal velocity. From the line center to ω_c, the collision operator is essentially frequency independent, limiting the impact regime.

The collective properties of the electrons are usually assumed to occur in a time that corresponds to the inverse of the electron plasma frequency $\omega_p = \sqrt{4\pi N_e e^2/m_e}$. However, if any process reduces the characteristic duration of the perturbation, the correlation can be considered lost. This is the case, for example, for high-n series lines of hydrogen, studied for plasma conditions relevant to magnetic fusion and gas discharges experiments, where the line widths are larger than the plasma frequency.[59] It is also the case for plasmas with high density ($N_e \geqslant 10^{18}$ cm^{-3}) but relatively low temperature ($T_e \approx 1$ eV). Because of the large number of electrons in the Debye sphere, the correlation is lost when the electron configuration changes, i.e., when the electrons move. We use the inverse time corresponding to a configuration change, $\omega_e = 2\pi/\tau_e$, where the characteristic time of the interaction is $\tau_e = r_e/v_{th}$. Moreover, as mentioned in Sec. III, it has been shown that introducing helical trajectories reduces the characteristic duration of the perturbation to the order of the inverse of the Larmor frequency. In this case, a cutoff at $\omega_L = eB/m_e c$ should be used.[60] Finally, for non-degenerated systems, an additional cutoff at frequency $\omega_{\alpha\alpha'}$ between the states α and α' has also been retained.[44] Hence, the cutoff frequency ω_c in Eq. (20) has been modified in PPPB to account for electron–electron correlations and helical trajectories. Here, we have $\omega_c = \max(\omega_p, \omega_e, \omega_L, \omega_{\alpha\alpha'})$.

How the Larmor frequency variation influences $G(\Delta\omega)$ is shown in Fig. 2 for conditions relevant to white-dwarf atmospheres (Lyman-α line at $N_e = 10^{17}$ cm^{-3}, $T_e = 5$ eV, and $B = 100$, 500, and 10^3 T). $G(\Delta\omega)$ calculated for $B = 100$ T is superposed on the non-magnetized results because ω_e is larger than ω_L for these plasma conditions. For higher B-field values, the cutoff is at the Larmor frequency. As the B-field value increases, the value of $G(\Delta\omega = 0)$ decreases as well as the derivative of this function. The impact region is then extended. Such results lead to a reduction of the SZ linewidth with increasing B.[40]

The impact limit $G(\Delta\omega = 0)$ is generally used in PPPB. It has been checked that for multicharged ions, this approximation affects only the wing of the lines for values of ω of the order of or larger than v_{th}/r_W ($r_W = \hbar n^2/Zmv_{th}$ being the Weisskopf radius).

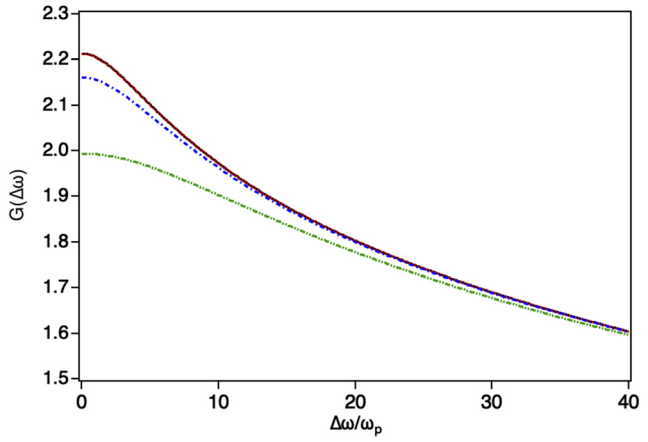

FIG. 2. $G(\Delta\omega)$ calculated for hydrogen Lyman-α line at $N_e = 10^{17}$ cm^{-3} and $T_e = 5$ eV for different B-field values that modify the cutoff frequency ω_L: $B = 100$ T (short-dash), $B = 500$ T (dot-dash), and $B = 1$ kT (double-dot-dash). For comparison, the $G(\Delta\omega)$ functions are shown for the non-magnetized case (solid line).

V. SELECTED APPLICATIONS

In this section, we present different examples of applications in a broad band of plasma conditions encountered in dense gas jet discharges and laser-produced plasma experiments in which strong, controlled, static magnetic fields could be generated, as for example by the capacitor–coil target technique.[61–63] In this technique, two

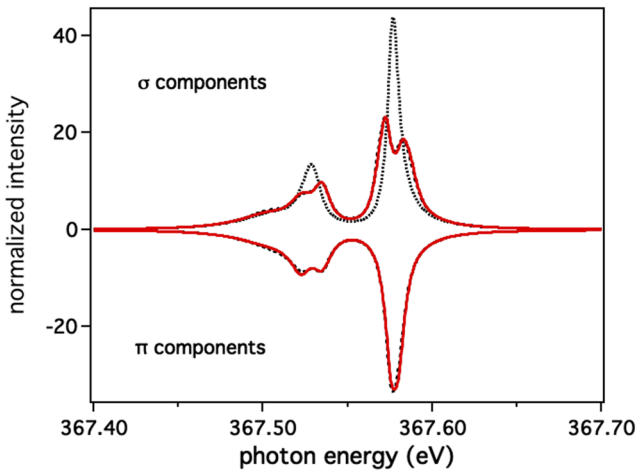

FIG. 3. SZ Lyman-α line profiles of C VI, using the weak-field (dashed) and intermediate-field (solid) approximations for $B = 100$ T, $N_e = 5 \times 10^{19}$ cm^{-3}, $T_e = 100$ eV. The short-dashed line corresponds to the pure Stark profile.

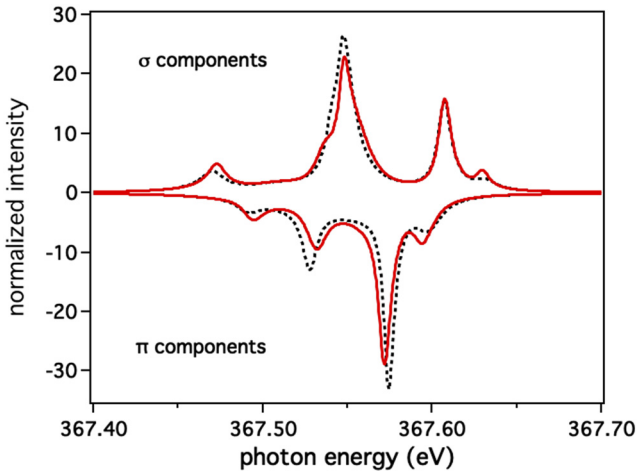

FIG. 4. As Fig. 3 but for $B = 500$ T.

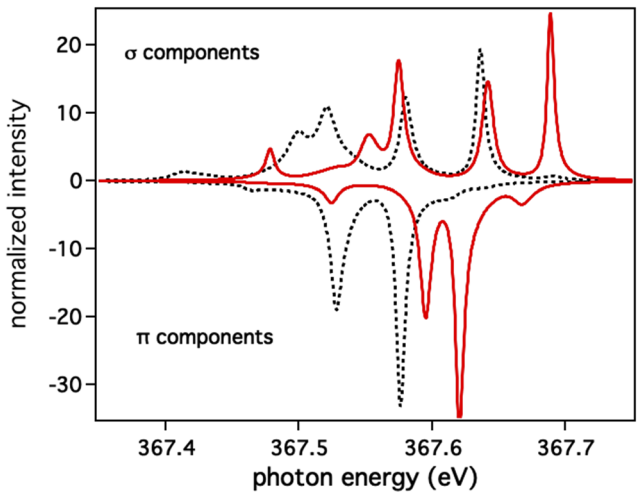

FIG. 5. As Fig. 3 but for $B = 10^3$ T.

parallel disks linked by a coil are irradiated by a high-power nanosecond laser: escaping hot electrons charge the target, giving rise to a strong current passing through the coil, and this strong current generates sub-nanosecond-duration B-fields of strength up to 1 kT.

A. Lyman-α lines of hydrogen-like carbon in dense laser-produced plasmas subjected to strong external magnetic fields: A need to account for intermediate B-fields

We investigate the SZ effect on the C VI Lyman-α line at 367.55 eV in a dense laser-produced plasma subjected to a strong external magnetic field. For the selected plasma conditions ($N_e = 10^{19}$–10^{20} cm^{-3} and $T_e = 100$ eV), the Stark broadening is less than 0.02 eV, and the fine structure of the line—corresponding to a splitting of 0.05 eV—can be seen. Such lines are interesting because under a magnetic field of the order of a few hundred teslas, the Zeeman splitting is sufficiently strong to prevail over the Stark broadening effect and moreover, none of the weak- or strong-field approximations are valid. Calculation of the atomic physics in the intermediate-B-field approximation is required.

Figures 3–5 show the SZ-broadened polarized profiles for three different B-fields. They are calculated using atomic data generated within the weak-field approximation (black line) or within the intermediate-field approximation (MASCB, red line). For the sake of clarity, the π components are plotted with negative intensities. The pure Stark profiles (dotted black line) are also plotted to show the modification due to the Zeeman effect on those lines. For $B = 100$ T, both approximations give largely the same Zeeman splitting and the profiles are mostly identical. For $B = 500$ T, the weak-field approximation starts to be critical and differences appear in the SZ line shapes. For $B = 10^3$ T, the Zeeman splitting being of the order of magnitude of the spin–orbit interaction, the weak-field approximation gives a drastically different B-field signature on the spectrum compared to the intermediate approximation. Using the latter, one can see a global blue-shift of the lines and different structures. In the limit of strong fields, e.g., $B \sim 10^4$ T, it has been checked that the spectra calculated with the intermediate-B-field approximation tend to those calculated with the strong-field approximation, in which the spin–orbit interaction is neglected.

B. Lithium-like isoelectronic C IV, N V, and O VI $n = 4$ to $n = 5$ lines subjected to strong external magnetic fields

Measurements of Stark-broadened profiles of the $n = 4$ to $n = 5$ transitions for lithium-like isoelectronic sequences have been reported in Ref. 64. They were observed in a gas-liner pinch discharge, where the plasma conditions of 10^{18} cm$^{-3} \leqslant N_e \leqslant 2.8 \times 10^{18}$ cm^{-3} and 8.6 eV $\leqslant T_e \leqslant$ 17 eV were diagnosed independently by Thomson scattering. The spectrometer resolution was sufficiently high to resolve the Stark-broadened profiles well, and the width of the apparatus profile was 3%, 25%, and 43% of the Stark-broadened C IV, N V, and O VI $n = 4$ to

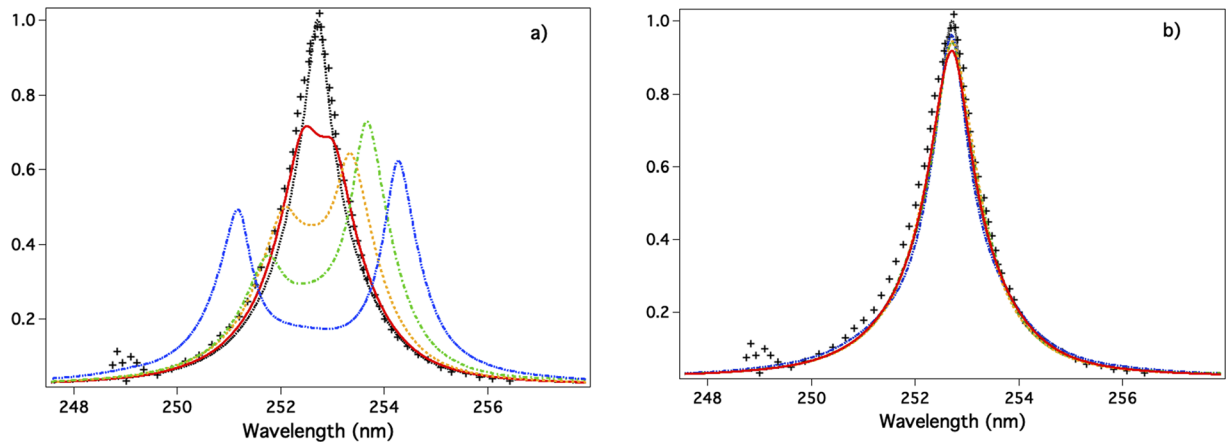

FIG. 6. SZ C IV $n = 4$ to $n = 5$ polarized line profiles for $N_e = 2 \times 10^{19}$ cm^{-3}, $T = 10$ eV, $B = 0$ (dot), $B = 100$ T (solid), $B = 200$ T (dash), $B = 300$ T (dot-dash), and $B = 500$ T (double-dot-dash): (a) σ components; (b) π components. The experimental results[64] are plotted with solid plus signs.

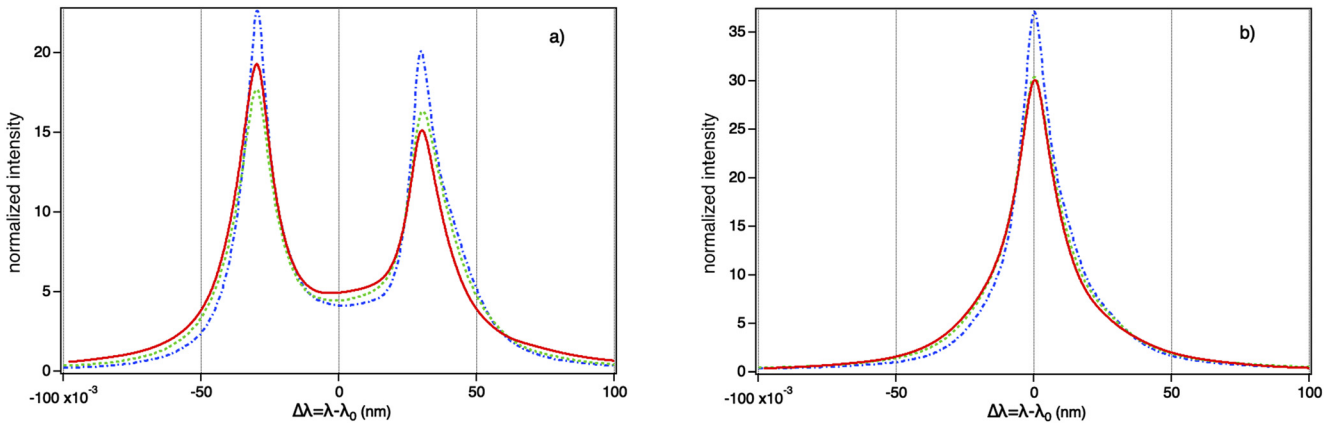

FIG. 7. Comparisons of SZ-broadened $n = 4$ to $n = 5$ line transitions for C IV (solid), N V (dash), and O VI (dot-dash) at $B = 500$ T, $N_e = 2 \times 10^{18}$ cm^{-3}, $T_e = 10$ eV: (a) σ components; (b) π components.

$n = 5$ transition linewidths, respectively. Furthermore, the width of the corresponding Doppler profiles was below 0.1% in all cases. The experimental setup described in Ref. 64 provided a benchmark for models. We have investigated the effects of strong B-fields on those lines.

SZ calculations are challenging here because the number of fine-structure energy levels, the line transitions, and the Stark coupling between energy levels increase with the PQN. For the present calculations, levels belonging to $n = 4$, 5 and 6 have been considered. In total, 154 fine-structure energy levels associated with the upper (initial) levels and 32 fine-structure energy levels associated with the lower (final) ones are then accounted for, and over 1200 electric-dipole-allowed transitions are accounted for in the calculations (including $\Delta n \neq 0$).

Figure 6 shows the modifications of the calculated C IV $n = 4$ to $n = 5$ line shapes under magnetic fields up to $B = 500$ T for $N_e = 2 \times 10^{18}$ cm^{-3} and $T_e = T_i = 10$ eV. In both subfigures, the pure Stark-broadened line profile, i.e., the $B = 0$ calculation, is plotted together with the measured one to illustrate the very good agreement between PPP and the experimental data (taken from Ref. 64). The Zeeman patterns of the $n = 4$ to $n = 5$ line transitions show interesting features because the line shapes corresponding to the σ components present two distinguishable peaks that split as the B-field increases, whereas the SZ line shapes corresponding to the π components do not really vary with B-field values.

A similar tendency is seen for the SZ line shapes of lithium-like nitrogen and oxygen. Figure 7 shows the SZ effect on the σ and π components of the C IV, N V, and O VI $n = 4$ to $n = 5$ transitions.

By recording experimentally the σ and π components simultaneously, it is possible to characterize the polarization degree of the different SZ emission lines:

$$P(\omega) = \frac{I_\pi(\omega) - I\sigma(\omega)}{I_\pi(\omega) + I\sigma(\omega)}. \tag{21}$$

Figure 8 shows the polarization degree calculated for the C IV $n = 4$ to $n = 5$ transitions for different B-field values. As the π and σ components present very different line profiles, the variation of the polarization degree reaches 70%. This case is very favorable for inferring the magnetic field because the Zeeman patterns are observed well among the Stark broadening. Nevertheless, for cases in which the Zeeman patterns tend to be masked by other broadening mechanisms, polarization degrees of a few percent can still be measured experimentally.[65]

Figure 9 shows the σ and π SZ line shapes of the O VI $n = 4$ to $n = 5$ transitions calculated for a magnetic field of $B = 100$ T and convolved with a Lorentzian apparatus profile with a full width at half maximum of 0.18 nm, corresponding to the detection system used in Ref. 64. Accounting for this additional broadening, the σ components are no longer resolved and show a profile similar to that of the π components. A measurement of the B-field from the Zeeman patterns would be unreliable, whereas it would still be feasible using the corresponding polarization degree that gives 5% at the center of the line. Comparing

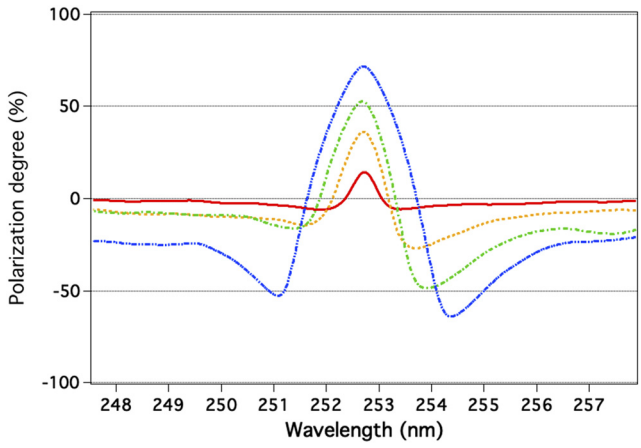

FIG. 8. Polarization degree of C IV $n = 4$ to $n = 5$ lines for $N_e = 2 \times 10^{18}$ cm^{-3}, $T_e = 10$ eV, $B = 100$ T (solid), $B = 200$ T (dash), $B = 300$ T (dot-dash), and $B = 500$ T (double-dot-dash).

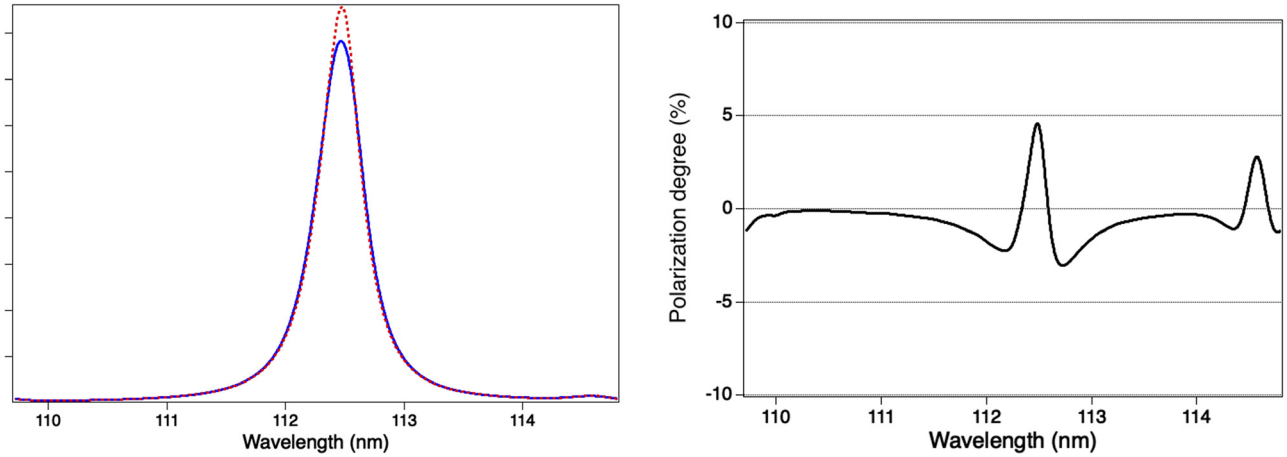

FIG. 9. SZ line shapes, σ (solid) and π (dash) components, and corresponding polarization degree of O VI $n = 4$ to $n = 5$ lines for $B = 100$ T at $N_e = 2 \times 10^{18}$ cm^{-3} and $T_e = 10$ eV.

the observed and calculated polarization degree can then in principle be used as a diagnostic tool to infer the magnetic field even if the Zeeman patterns are masked.

C. Ar K-shell emission in strongly magnetized plasmas

The design of a novel all-optical platform for magnetizing laser-driven cylindrical implosions at the OMEGA facility and their characterization through x-ray line emission has recently been proposed.[66,67] The experimental scheme combines the laser-driven MagLIF configuration for the implosion of low-density gas-filled cylindrical targets[68] with laser-driven seed B-fields.[63] A B-field exceeding 10 kT over the entire compressed core is predicted by the MHD code GORGON.[69,70] For the referred conditions, Ar K-shell spectra are expected to be observed thanks to the high-quality spectroscopic data for Ar K-shell emission lines—with a spectral resolution of $E/\Delta E \sim 1800$—already obtained in inertial-confinement-fusion experiments.[71,72]

Three spectral properties of dopant atoms can be exploited to infer a unique measurement of the core electron temperature and density as well as the local B-field: (i) the Stark-broadened line shapes, which depend strongly on the electron density, (ii) the relative intensity distribution of K-shell lines and associated satellites, which are sensitive to the electron temperature and density,[72] and (iii) the expected compressed B-field, which is indeed strong enough to induce significant splitting, broadening, and polarization effects on the K-shell emission spectra.[17]

We have investigated the SZ-broadened line shapes of Ar K-shell x-ray transitions in hydrogen- and helium-like ions, i.e., Ly$_\alpha$ ($2p \rightarrow 1s$), Ly$_\beta$ ($3p \rightarrow 1s$), Ly$_\gamma$ ($4p \rightarrow 1s$), and Ly$_\delta$ ($5p \rightarrow 1s$) in H-like Ar and He$_\alpha$ ($1s2p \rightarrow 1s^2$), He$_\beta$ ($1s3p \rightarrow 1s^2$), and He$_\gamma$ ($1s4p \rightarrow 1s^2$) in He-like Ar. Here, a tracer amount of Ar in a deuterium plasma was considered, and a grid of plasma densities from $N_e = 3 \times 10^{22}$ cm^{-3} to 3×10^{24} cm^{-3} and a grid of B-field values from 10 to 80 kT were used. Because the Stark-broadened line shapes depend weakly on the electron temperature, only a

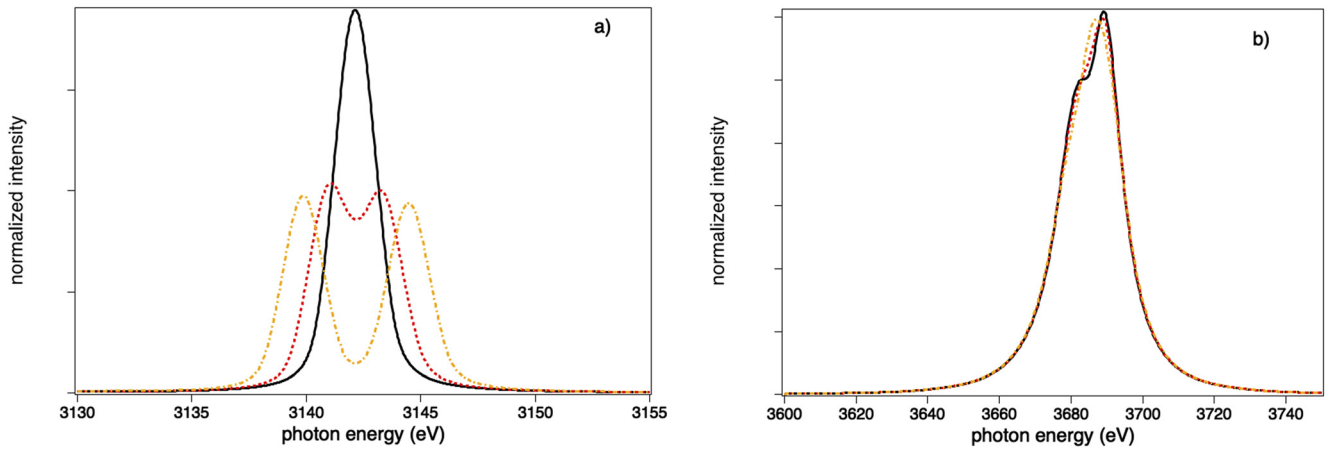

FIG. 10. Calculations of (a) Ar He-α and (b) He-β SZ spectral lines for $N_e = 5 \times 10^{23}$ cm^{-3}, $T_e = 2$ keV, $B = 0$ (solid), $B = 20$ kT (dash), and $B = 40$ kT (dot-dash). A convolution with an instrumental resolution of $E/\Delta E = 1800$ is performed, and the observation is parallel to the magnetic field.

representative value of 2 keV was chosen. Such detailed SZ line shapes were used in the NLTE atomic kinetics code ABAKO[73] to compute synthetic x-ray emission spectra.[17,67]

In Fig. 10, the SZ line shapes of the Ar He-α and He-β calculated for two B-fields values (B = 20 and 40 kT) are compared to the corresponding Stark-broadened profiles (B = 0). The Doppler and instrumental resolution of $E/\Delta E$ = 1800 is accounted for. As shown in the figure, the He-α line is more sensitive than the He-β line in terms of Zeeman splitting. The same tendency has been seen for the Ar H-like Lyman lines. As the PQN increases, the Stark broadening increases and masks the Zeeman patterns.

A possible way to measure the plasma parameters from the synthetic spectra would be as follows. By measuring different emission lines simultaneously, one could characterize the plasma density and temperature from the β lines through the Stark broadening. For the found plasma parameters, one could adjust the B-field value needed to reproduce the extra B-field-induced broadening observed in experimental α lines. Although the He-α lines suffer from re-absorption for such plasma conditions, the latter occurs in the center of the line. As the Zeeman effect splits the lines, one can expect that the sigma components will be poorly re-absorbed, thereby making the B-field diagnostic still feasible.

VI. CONCLUSION

Atomic structure can be used to characterize magnetized plasmas because hydrogen and multi-ionized-atom line emissions broaden and become polarized under strong B-fields. In this paper, the main features of the SZ line-shape code PPPB were presented through various applications related to strongly magnetized plasmas encountered in either astrophysics or the laboratory. PPPB allows calculations over a wide range of plasma conditions and is sufficiently fast to provide line shapes for use in radiation transport codes. The Zeeman effect in intermediate coupling is accounted for by the atomic-physics code MASCB that generates B-field-dependent atomic-physics quantities. Investigations of hydrogen line series in highly magnetized astrophysical plasmas have shown that the quadratic Zeeman terms give rise to additional structures and to a global shift that increases with the PQN. In high-energy-density plasmas, measuring gigagauss (10^5 T) magnetic fields using Zeeman-broadened lines from highly charged ions has been proposed,[74] and investigating how the quadratic terms affect the SZ line shapes emitted from highly charged ions may be very important because those lines are used as diagnostic tools.

Another interesting study is how helical trajectories affect charged particles produced in the presence of strong B-fields. The gyromotion of ions and electrons may alter the dynamics of the plasma particles and thus their interaction with the plasma emitters. The present version of the code accounts for this effect by using a cutoff at the Larmor frequency in the electron broadening operator. The effects of anisotropy and screening on the electronic and ionic microfield properties must be investigated to improve the corresponding models in line-shape codes.

ACKNOWLEDGMENTS

This work was supported by the EUROfusion Enabling Research work programme 2017 (Grant No. CfP-AWP17-IFE-CEA-02).

AUTHOR DECLARATIONS

Conflict of Interest

The authors have no conflicts to disclose.

DATA AVAILABILITY

The data that support the findings of this study are available from the corresponding author upon reasonable request.

REFERENCES

[1]H. R. Griem, *Principles of Plasma Spectroscopy* (Cambridge University Press, Cambridge, 1997).
[2]H. Nguyen-Hoe, H.-W. Drawin, and L. Herman, "Effet d'un champ magnetique uniforme sur les profils des raies de l'hydrogene," J. Quant. Spectrosc. Radiat. Transfer **7**, 429–474 (1967).
[3]M. S. Murillo, M. E. Cox, and S. M. Carr, "Magnetized plasma microfield studies by molecular dynamics simulation," J. Quant. Spectrosc. Radiat. Transfer **58**, 811–820 (1997).
[4]M. A. Gigosos and M. Á. González, "Comment on 'A study of ion-dynamics and correlation effects for spectral line broadening in plasma: K-shell lines,'" J. Quant. Spectrosc. Radiat. Transfer **105**, 533–535 (2007).
[5]E. Stambulchik, K. Tsigutkin, and Y. Maron, "Spectroscopic method for measuring plasma magnetic fields having arbitrary distributions of direction and amplitude," Phys. Rev. Lett. **98**, 225001 (2007).
[6]J. Rosato, D. Reiter, V. Kotov, P. Börner, H. Capes, Y. Marandet, R. Stamm, S. Ferri, L. Godbert-Mouret, M. Koubiti *et al.*, "Line shape modeling for radiation transport investigations in magnetic fusion plasmas," High Energy Density Phys. **5**, 93–96 (2009).
[7]G. Mathys, "The transfer of polarized light in Stark broadened hydrogen lines in the presence of a magnetic field," J. Quant. Spectrosc. Radiat. Transfer **44**, 143–151 (1990).
[8]A. Derevianko and E. Oks, "Generalized theory of ion impact broadening in magnetized plasmas and its applications for tokamaks," Phys. Rev. Lett. **73**, 2059 (1994).
[9]S. Brillant, G. Mathys, and C. Stehle, "Hydrogen line formation in dense magnetized plasmas," Astron. Astrophys. **339**, 286–297 (1998).
[10]S. Günter and A. Könies, "Diagnostics of dense plasmas from the profile of hydrogen spectral lines in the presence of a magnetic field," J. Quant. Spectrosc. Radiat. Transfer **62**, 425–431 (1999).
[11]L. Godbert-Mouret, M. Koubiti, R. Stamm, K. Touati, B. Felts, H. Capes, Y. Corre, R. Guirlet, and C. De Michelis, "Spectroscopy of magnetized plasmas," J. Quant. Spectrosc. Radiat. Transfer **71**, 365–372 (2001).
[12]M. L. Adams, R. W. Lee, H. A. Scott, H. K. Chung, and L. Klein, "Complex atomic spectral line shapes in the presence of an external magnetic field," Phys. Rev. E **66**, 066413 (2002).
[13]X.-d. Li, S.-s. Han, C. Wang, and Z.-z. Xu, "Ultrahigh magnetic field diagnostic with spectral profile calculation," J. Quant. Spectrosc. Radiat. Transfer **76**, 31–43 (2003).
[14]S. Ferri, A. Calisti, C. Mossé, L. Mouret, B. Talin, M. A. Gigosos, M. A. González, and V. Lisitsa, "Frequency-fluctuation model applied to Stark–Zeeman spectral line shapes in plasmas," Phys. Rev. E **84**, 026407 (2011).
[15]C. A. Iglesias, "Efficient algorithms for Stark–Zeeman spectral line shape calculations," High Energy Density Phys. **9**, 737–744 (2013).
[16]F. Gilleron and J.-C. Pain, "ZEST: A fast code for simulating Zeeman-Stark line-shape functions," Atoms **6**, 11 (2018).
[17]J. J. Santos, M. Bailly-Grandvaux, M. Ehret, A. V. Arefiev, D. Batani, F. N. Beg, A. Calisti, S. Ferri, R. Florido, P. Forestier-Colleoni *et al.*, "Laser-driven strong magnetostatic fields with applications to charged beam transport and magnetized high energy-density physics," Phys. Plasmas **25**, 056705 (2018).
[18]C. Liu, K. Matsuo, S. Ferri, H.-K. Chung, S. Lee, S. Sakata, K. F. F. Law, H. Morita, B. Pollock, J. Moody *et al.*, "Design of Zeeman spectroscopy experiment with

magnetized silicon plasma generated in the laboratory," High Energy Density Phys. **33**, 100710 (2019).
[19]R. D. Cowan, *The Theory of Atomic Structure and Spectra* (University of California Press, 1981), Vol. 3.
[20]I. P. Grant, B. J. McKenzie, P. H. Norrington, D. F. Mayers, and N. C. Pyper, "An atomic multiconfigurational Dirac-Fock package," Comput. Phys. Commun. **21**, 207–231 (1980).
[21]M. F. Gu, "The flexible atomic code," Can. J. Phys. **86**, 675–689 (2008).
[22]E. Stambulchik, cFAC code in GitHub kernel description, https://github.com/fnevgeny/cfac (last accessed 11/23/2021)
[23]B. Cagnac and J. C. P. Peyroula, *Physique Atomique, Tome 2: Applications de la Mecanique Quantique* (Bordas, 1982).
[24]J. C. Slater, *Quantum Theory of Atomic Structure*, McGraw-Hill (1960).
[25]M. S. Litsarev and O. V. Ivanov, "Multiconfiguration Hartree-Fock method: Direct diagonalization for the construction of a multielectron basis," J. Exp. Theor. Phys. **111**, 22–26 (2010).
[26]E. G. Hill, "Calculation of unit tensor operators using a restricted set of slater determinants," J. Quant. Spectrosc. Radiat. Transfer **140**, 1–6 (2014).
[27]E. U. Condon, E. Condon, and G. Shortley, *The Theory of Atomic Spectra* (Cambridge University Press, 1935).
[28]J. D. Talman and W. F. Shadwick, "Optimized effective atomic central potential," Phys. Rev. A **14**, 36 (1976).
[29]J. B. Krieger, Y. Li, and G. J. Iafrate, "Systematic approximations to the optimized effective potential: Application to orbital-density-functional theory," Phys. Rev. A **46**, 5453 (1992).
[30]R. H. Garstang and S. B. Kemic, "Hydrogen and helium spectra in large magnetic fields," Astrophys. Space Sci. **31**, 103–115 (1974).
[31]S. O. Kepler, I. Pelisoli, S. Jordan, S. J. Kleinman, D. Koester, B. Külebi, V. Peçanha, B. G. Castanheira, A. Nitta, J. E. S. Costa *et al.*, "Magnetic white dwarf stars in the sloan digital sky survey," Mon. Not. R. Astron. Soc. **429**, 2934–2944 (2013).
[32]J. Rosato, "Hydrogen line shapes in plasmas with large magnetic fields," Atoms **8**, 74 (2020).
[33]A. Raji, J. Rosato, R. Stamm, and Y. Marandet, "New analysis of Balmer line shapes in magnetic white dwarf atmospheres," Eur. Phys. J. D **75**(2), 1–4 (2021).
[34]D. R. Inglis and E. Teller, "Ionic depression of series limits in one-electron spectra," Astrophys. J. **90**, 439 (1939).
[35]T. Ott and M. Bonitz, "Diffusion in a strongly coupled magnetized plasma," Phys. Rev. Lett. **107**, 135003 (2011).
[36]S. D. Baalrud and J. Daligault, "Transport regimes spanning magnetization-coupling phase space," Phys. Rev. E **96**, 043202 (2017).
[37]D. J. Bernstein, T. Lafleur, J. Daligault, and S. D. Baalrud, "Friction force in strongly magnetized plasmas," Phys. Rev. E **102**, 041201 (2020).
[38]E. Oks, "Influence of magnetic-field-caused modifications of trajectories of plasma electrons on spectral line shapes: Applications to magnetic fusion and white dwarfs," J. Quant. Spectrosc. Radiat. Transfer **171**, 15–27 (2016).
[39]J. Rosato, S. Ferri, and R. Stamm, "Influence of helical trajectories of perturbers on Stark line shapes in magnetized plasmas," Atoms **6**, 12 (2018).
[40]S. Alexiou, "Line shapes in a magnetic field: Trajectory modifications I: Electrons," Atoms **7**, 52 (2019).
[41]S. Alexiou, "Line shapes in a magnetic field: Trajectory modifictions II: Full collision-time statistics," Atoms **7**, 94 (2019).
[42]C. Deutsch, "Electric microfield distributions in plasmas in presence of a magnetic field," Phys. Lett. A **30**, 381–382 (1969).
[43]S. Ferri, "Study of plasma microfield properties in highly magnetized plasmas" (unpublished) (2018), see https://pnp16.sciencesconf.org/207981/document.
[44]A. Calisti, F. Khelfaoui, R. Stamm, B. Talin, and R. W. Lee, "Model for the line shapes of complex ions in hot and dense plasmas," Phys. Rev. A **42**, 5433 (1990).
[45]A. Calisti, L. Godbert, R. Stamm, and B. Talin, "Fast numerical methods for line shape studies in hot and dense plasmas," J. Quant. Spectrosc. Radiat. Transfer **51**, 59–64 (1994).
[46]N. C. Woolsey, A. Asfaw, B. Hammel, C. Keane, C. A. Back, A. Calisti, C. Mossé, R. Stamm, B. Talin, J. S. Wark *et al.*, "Spectroscopy of compressed high energy density matter," Phys. Rev. E **53**, 6396 (1996).
[47]N. C. Woolsey, B. A. Hammel, C. J. Keane, A. Asfaw, C. A. Back, J. C. Moreno, J. K. Nash, A. Calisti, C. Mossé, R. Stamm *et al.*, "Evolution of electron temperature and electron density in indirectly driven spherical implosions," Phys. Rev. E **56**, 2314 (1997).
[48]B. Talin, A. Calisti, L. Godbert, R. Stamm, R. W. Lee, and L. Klein, "Frequency-fluctuation model for line-shape calculations in plasma spectroscopy," Phys. Rev. A **51**, 1918 (1995).
[49]M. Abramowitz and I. Stegun, *Handbook of Mathematical Functions* (US GPO, 1972), Vol. 55.
[50]B. Talin, E. Dufour, A. Calisti, M. A. Gigosos, M. A. González, T. del Rio Gaztelurrutia, and J. W. Dufty, "Molecular dynamics simulation for modelling plasma spectroscopy," J. Phys. A: Math. Gen. **36**, 6049 (2003).
[51]C. A. Iglesias, H. E. DeWitt, J. L. Lebowitz, D. MacGowan, and W. B. Hubbard, "Low-frequency electric microfield distributions in plasmas," Phys. Rev. A **31**, 1698 (1985).
[52]C. A. Iglesias, F. J. Rogers, R. Shepherd, A. Bar-Shalom, M. S. Murillo, D. P. Kilcrease, A. Calisti, and R. W. Lee, "Fast electric microfield distribution calculations in extreme matter conditions," J. Quant. Spectrosc. Radiat. Transfer **65**, 303–315 (2000).
[53]C. F. Hooper, Jr., "Low-frequency component electric microfield distributions in plasmas," Phys. Rev. **165**, 215 (1968).
[54]N. C. Woolsey, B. A. Hammel, C. J. Keane, C. A. Back, J. C. Moreno, J. K. Nash, A. Calisti, C. Mossé, L. Godbert, R. Stamm *et al.*, "Spectroscopic line shape measurements at high densities," J. Quant. Spectrosc. Radiat. Transfer **58**, 975–989 (1997).
[55]S. Ferri, A. Calisti, C. Mossé, J. Rosato, B. Talin, S. Alexiou, M. A. Gigosos, M. González, D. González-Herrero, N. Lara *et al.*, "Ion dynamics effect on Stark-broadened line shapes: A cross-comparison of various models," Atoms **2**, 299–318 (2014).
[56]A. Calisti, C. Mossé, S. Ferri, B. Talin, F. Rosmej, L. A. Bureyeva, and V. S. Lisitsa, "Dynamic Stark broadening as the Dicke narrowing effect," Phys. Rev. E **81**, 016406 (2010).
[57]H. R. Griem, M. Blaha, and P. C. Kepple, "Stark-profile calculations for Lyman-series lines of one-electron ions in dense plasmas," Phys. Rev. A **19**, 2421 (1979).
[58]E. Galtier, F. Rosmej, A. Calisti, B. Talin, C. Mossé, S. Ferri, and V. Lisitsa, "Interference effects and Stark broadening in XUV intrashell transitions in aluminum under conditions of intense XUV free-electron-laser irradiation," Phys. Rev. A **87**, 033424 (2013).
[59]S. Ferri, A. Calisti, R. Stamm, B. Talin, R. W. Lee, and L. Klein, "Electronic broadening model for high-n balmer line profiles," Phys. Rev. E **58**, R6943(R) (1998).
[60]E. Maschke and D. Voslamber, "Stark broadening of hydrogen lines in strong magnetic fields," in Proceedings of the 7th International Conference on Phenomena in Ionized Gases (1966), Vol. II, p. 568.
[61]H. Daido, F. Miki, K. Mima, M. Fujita, K. Sawai, H. Fujita, Y. Kitagawa, S. Nakai, and C. Yamanaka, "Generation of a strong magnetic field by an intense CO_2 laser pulse," Phys. Rev. Lett. **56**, 846 (1986).
[62]S. Fujioka, Z. Zhang, K. Ishihara, K. Shigemori, Y. Hironaka, T. Johzaki *et al.*, "Kilotesla magnetic field due to a capacitor-coil target driven by high power laser," Sci. Rep. **3**(1), 1–7 (2013).
[63]J. J. Santos, M. Bailly-Grandvaux, L. Giuffrida, P. Forestier-Colleoni, S. Fujioka, Z. Zhang, P. Korneev, R. Bouillaud, S. Dorard, D. Batani *et al.*, "Laser-driven platform for generation and characterization of strong quasi-static magnetic fields," New J. Phys. **17**, 083051 (2015).
[64]S. Glenzer, T. Wrubel, S. Buscher, H.-J. Kunze, L. Godbert, A. Calisti, R. Stamm, B. Talin, J. Nash, R. W. Lee *et al.*, "Spectral line profiles of n = 4 to n = 5 transitions in C IV, N V and O VI," J. Phys. B: At., Mol. Opt. Phys. **27**, 5507 (1994).
[65]T. Fujimoto and A. Iwamae, *Plasma Polarization Spectroscopy* (Springer, 2008), Vol. 44.
[66]M. Bailly-Grandvaux, S. McGuffey, F. Beg, S. Ferri, A. Calisti, J. Davies, R. Florido, M. Gigosos, J. Honrubia, R. Mancini *et al.*, "An all-optical platform to characterize strongly magnetized hot dense plasmas at >10 kT," in *APS Division of Plasma Physics Meeting Abstracts*, (2020), Vol. 2020, p. BO07–005.
[67]R. Florido, C. Walsh, M. Bailly-Grandvaux, F. Beg, C. McGuffey, A. Calisti, S. Ferri, M. Gigosos, R. Mancini, T. Nagayama *et al.*, "Spectroscopic and MHD modeling of magnetized cylindrical implosions using a laser-produced seed B-

field," in APS Divisi on of *Plasma Physics Meeting Abstracts*, (2020), Vol. 2020, p. GP17.00009.
[68]J. R. Davies, D. H. Barnak, R. Betti, E. M. Campbell, V. Y. Glebov, E. C. Hansen, J. P. Knauer, J. L. Peebles, and A. B. Sefkow, "Inferring fuel areal density from secondary neutron yields in laser-driven magnetized liner inertial fusion," Phys. Plasmas **26**, 022706 (2019).
[69]C. A. Walsh, K. McGlinchey, J. K. Tong, B. D. Appelbe, A. Crilly, M. F. Zhang, and J. P. Chittenden, "Perturbation modifications by pre-magnetisation of inertial confinement fusion implosions," Phys. Plasmas **26**, 022701 (2019).
[70]C. A. Walsh, J. P. Chittenden, D. W. Hill, and C. Ridgers, "Extended-magnetohydrodynamics in under-dense plasmas," Phys. Plasmas **27**, 022103 (2020).
[71]N. C. Woolsey, B. A. Hammel, C. J. Keane, C. A. Back, J. C. Moreno, J. K. Nash, A. Calisti, C. Mossé, R. Stamm, B. Talin *et al.*, "Competing effects of collisional ionization and radiative cooling in inertially confined plasmas," Phys. Rev. E **57**, 4650 (1998).
[72]H.-K. Chung and R. W. Lee, "Applications of NLTE population kinetics," High Energy Density Phys. **5**, 1–14 (2009).
[73]R. Florido, R. Rodríguez, J. M. Gil, J. G. Rubiano, P. Martel, E. Mínguez, and R. C. Mancini, "Modeling of population kinetics of plasmas that are not in local thermodynamic equilibrium, using a versatile collisional-radiative model based on analytical rates," Phys. Rev. E **80**, 056402 (2009).
[74]J. F. Seely, "Gigagauss magnetic field measurements using Zeeman broadening of Ne-like transitions in highly charged ions," Rev. Sci. Instrum. **92**, 053535 (2021).